First-principles study of the biomineral hydroxyapatite

Alexander Slepko and Alexander A. Demkov*
Department of Physics, The University of Texas at Austin, Austin, Texas 78712, USA
(Received 19 July 2011; published 19 October 2011)

The biomineral hydroxyapatite $Ca_{10}(PO_4)_6(OH)_2$ is the main mineral constituent of mammal bone. Hydroxyapatite crystallizes in the hexagonal and monoclinic phases, the main difference between them being the orientation of the hydroxyl groups. Using density functional theory, we study the energetics of the hexagonal and monoclinic phases, along with the several hypothetical crystal structures of hydroxyapatite. The monoclinic phase has the lowest energy, with the hexagonal phase being only 22 meV/cell higher in energy. We identify a structural transition path from the hexagonal to monoclinic phase, with the activation energy of 0.66 eV per hexagonal cell. At room temperature, the transition occurs on a millisecond time scale. The electronic structures of the monoclinic and hexagonal phases are compared. For the hexagonal phase, we calculate the phonon frequencies at the Γ-point and elastic constants. Both are in good agreement with available experimental results.

DOI: 10.1103/PhysRevB.84.134108 PACS number(s): 64.70.Nd, 62.23.St, 63.20.D−, 64.70.dg

I. INTRODUCTION

A carbonated form of hydroxyapatite $[Ca_{10}(PO_4)_6(OH)_2]$ is one of the most abundant materials in mammal bone.[1] It crystallizes within the free space between tropocollagen protein chains (Fig. 1) and strengthens the bone tissue. The mineral content of a typical human bone increases with age and reaches a maximum value in males and females at different ages.[2] From this peak value, the mineral content starts to decrease, leading to diseases such as (e.g., osteomalacia, softening of the bone caused by the loss of bone mineral). Some of the emergent applications of hydroxyapatite (HA) are, therefore, bone repair and replacement and production of synthetic bone material.[3] Although, by itself, HA is too brittle to be used as bone replacement directly, a variety of coating techniques have been developed in recent years to combine the strength of metals (such as titanium) with the natural bioactivity of HA.[4] The key property besides bio-activity is therefore HA adhesion to metals. Adhesion is governed by chemical bonding; thus, the problem is that of the electronic properties of the interface. Therefore, a thorough understanding of the electronic and mechanical properties of HA and its surface and interfaces to other substrates are of scientific interest.

A significant amount of experimental work on HA has been done, and for an excellent review of this work, in particular in the medical implant field, we refer the interested reader to Ref. 4. Some of the first experimental reports of HA date back to 1936.[5] In his work on dental enamel, Schmidt demonstrated that the crystallographic *c*-axes of the HA platelets within the collagen framework are well aligned with the collagen fibrils (Fig. 1). The hexagonal crystal structure of HA with $P6_3/m$ symmetry (#176 in the *International X-Ray Tables*, Fig. 2) and the atomic positions were determined in 1958 by Posner *et al.*[6] using X-ray diffraction In 1964, Kay and coworkers[7] refined the positions of the OH molecules using neutron diffraction. Studies of the alignment of tropocollagen chains in mammal bone and alignment and growth of HA crystals were done by Weiner and coworkers.[8] In the 1970s,[9] Carlisle showed that doping (in that study with Si) can play an important role in supporting bone growth. A monoclinic variant of HA was suggested in 1967 by Young.[10] He inferred that a HA crystal sufficiently free of impurities and vacancies could crystallize in the monoclinic phase analogous to the known monoclinic chlorapatite. Before this work, it was believed that HA only appeared in a hexagonal structure. Recently, the monoclinic variant of hydroxyapatite attracted significant interest (e.g., Refs. 11 and 12).

From the theoretical point of view, the HA crystal presents an interesting challenge because of its complexity and importance in biological and biophysical systems. Only with the recent increase in computational power has a theoretical study on HA become feasible, and of late, along with other calcium apatites, HA has been subject to a number of first-principles calculations. De Leeuw,[13] using density functional theory (DFT), analyzed the HA crystal structure and, specifically, the position and orientation of hydroxyl molecules. She suggests that the experimentally found OH disorder in the crystal is due to locally ordered domains with differently oriented OH molecules. In the simplest case, this is achieved in a monoclinic cell. Later, using DFT, Calderin *et al.*[14] have analyzed the crystal structure and electronic density of states of stoichiometric and OH-deficient HA, as well a variety of other calcium apatites. They found that monoclinic and hexagonal HA are very close in energy, indicating no particular preference for crystallization in a specific structure. They also found that apatites permit exchange of OH molecules with other anions. The electronic structure has been confirmed by Rulis and coworkers[15] using the orthogonalized linear combination of atomic orbitals method. More recently, studies have focused on altering the electronic and chemical properties of HA with doping. For example, Chappell and Bristowe[16] have studied the influence of substituting phosphorus with silicon on the HA crystal and electronic structure. Silicon incorporation is found to be energetically most favorable in combination with removing one of the two negatively charged OH pairs in the primitive cell to maintain the overall charge neutrality (the ionic charge of SiO_4 is -4 compared with -3 of a PO_4 unit). Other recent theoretical studies of doping include the substitution of OH by fluorine[17] (making the crystal a mixture of HA and flourapatite [FA]), introduction of carbonate ion (CO_3^{2-}) to study the physiologically found carbonated form of HA,[17] and calcium substitution by titanium[18] and strontium[19] to induce structural modifications. Using a classical shell

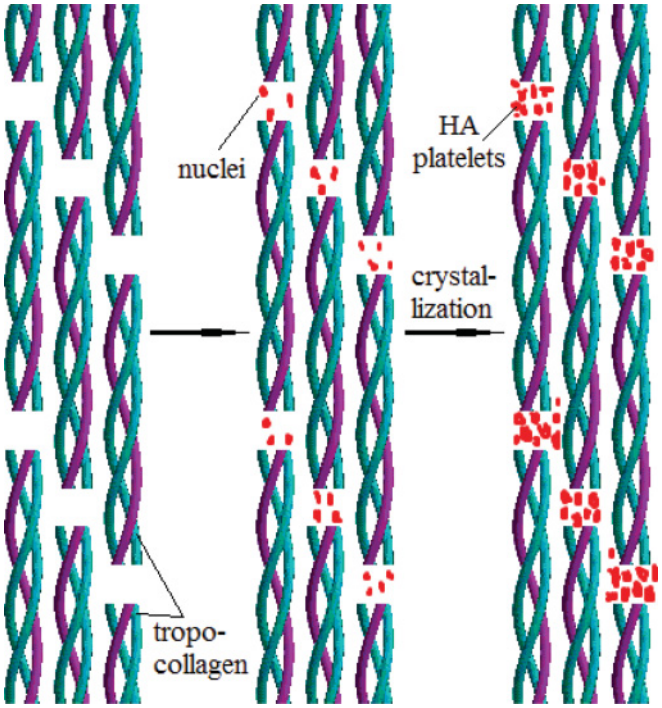

FIG. 1. (Color online) Schematic of the HA crystallization during bone formation. Experiments suggest that the *c*-axes of both the tropocollagen and HA platelets are aligned (Ref. 8). The formation of bone tissue happens in several steps. After the tropocollagen helices are aligned, constituents of the HA crystal accumulate in the spaces between the tropocollagen and crystallize in the (001) orientation. The final HA mineral within the spaces consists of many separate HA platelets.

model, Calderin *et al.*[20] investigated the lattice dynamics, calculated thermal factors, and simulated the infrared spectra of HA. They find good agreement with experimental results for the low-frequency and high-frequency vibrational modes at the Γ-point, whereas in the intermediate frequency range, the reported agreement is poor. More recently, classical and quantum mechanical molecular dynamics simulations have been used to study preferred surface orientations and terminations of HA[17,21,22] and to study water and amino acid adsorption on the HA surface.[17,21,23–25]

Despite recent progress, many questions remain. Little is known, for example, about transformation mechanisms between the hexagonal and monoclinic phases. The mechanical properties of HA remain virtually unstudied. HA is still a challenging subject for first-principles calculations due to a large number of atoms in the unit cells and a variation in the nature of interatomic bonding. In this paper, using density functional theory, we investigate both hexagonal and monoclinic forms of HA. We identify the monoclinic phase as the ground state and analyze possible pathways for the phase transition between the hexagonal and monoclinic phases. We carefully compare the electronic structure of both phases. For the hexagonal phase, we calculate the phonon frequencies at the Γ-point and elastic constants. Both are in good agreement with available experiment.

II. COMPUTATIONAL DETAILS

All calculations are done using density functional theory as implemented in VASP code.[26–30] We use the Perdew-Wang[31] (PW91) exchange correlation functional and projected augmented wave (PAW) pseudopotentials.[32] The valence configurations are $1s^1$ for hydrogen, $3s^2 3p^3$ for phosphorus, $4s^2$ for calcium, and $2s^2 2p^4$ for oxygen. We use 700 eV as the kinetic energy cutoff for bulk calculations. When calculating the phonon frequencies, we increase the energy cutoff to 950 eV to obtain highly accurate forces. In all calculations—except the elastic constant calculations—we allow for full relaxation of the cell, including changing the volume and adjusting the atomic positions and cell shape. When calculating the elastic constants, we only allow for the relaxation of ionic positions within the strained cells. Symmetry operations are switched off during relaxation. We use a $6 \times 6 \times 8$ Monkhorst–Pack[33] k-point mesh for the Brillouin Zone (BZ) integration of hexagonal cells that ensures the convergence to 1.8 meV/cell. For the monoclinic primitive cells, we use $6 \times 4 \times 6$ Monkhorst–Pack k-point meshes. All structures are relaxed until the largest force on atoms in the cell is smaller than 20 meV/Å. When calculating the vibrational modes, we relax the atomic positions until the largest force is smaller than 0.2 meV/Å.

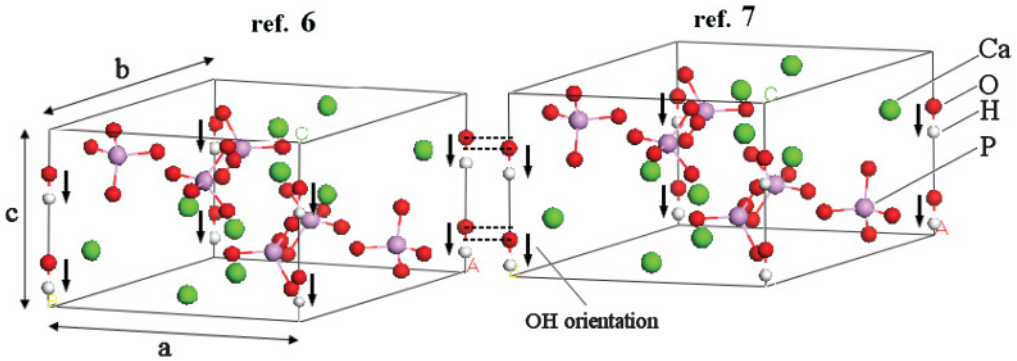

FIG. 2. (Color online) HA primitive cells as described in Refs. 6 and 7. The cell dimensions are $a = b = 9.432$ Å, $c = 6.881$ Å. The main difference between the two structures is the location of the oxygen atoms from the OH pairs as indicated in the figure. Following our notation (see text), we call the shown orientation of the OH pairs the (↓↓) orientation.

III. RESULTS

A. Ground state crystal structure

To identify the theoretical ground state of HA, we start from the experimental structure reported by Posner *et al.*[6] and Kay and Young[7] (as shown in Fig. 2). They report a hexagonal primitive cell of $P6_3/m$ symmetry (#176 in the *International X-Ray Tables*, Fig. 2) that contains 10 Ca atoms, six phosphate (PO_4) groups, and two hydroxyl (OH) molecules. In Fig. 3, we present a top view of the crystal. For pictorial purposes we shift the original primitive cell boundaries along the ***a*** and ***b*** axes in such a way that the OH column is now in the center of the cell. There are two types of Ca atoms in the cell. Ca atoms of one type are arranged in a hexagon around the OH molecules (Fig. 3). The darker and lighter colors distinguish two atomic planes. The darker balls are located at $z = 0.25c$, and the lighter ones are at $z = 0.75c$. The remaining four Ca atoms are arranged in two columns at the corners of the cell in Fig 3. In the upper left column, the two Ca_I atoms are located at $z = 0.999c$ and $z = 0.501c$. In the lower right column, the two remaining Ca_I atoms are located at $z = 0.499c$ and $z = 0.001c$. Similar to first type of Ca, six phosphorus atoms of PO_4 molecules are arranged in two triangles around the OH channel: three are at $z = 0.25c$ and three are at $z = 0.75c$. Again, the darker and lighter color in Fig. 3 distinguishes between the two planes. Although most of the atomic coordinates reported in Refs. 6 and 7 are almost exactly the same, the two structures differ in the position of the OH molecules. In Ref. 6, the exact positions of hydrogen atoms could not be determined, and the oxygen atoms are said to be located within the symmetry-related planes at $0.25c$ and $0.75c$. The later work[7] specifies the positions of hydrogen atoms and suggests that the oxygen of OH is shifted by ~0.3 Å along the c-axis with respect to the previously reported positions, as indicated in Fig. 2. The OH groups bring a structural ambiguity: two OH molecules do not have an energetic preference as to whether to point the hydrogen atom "upward" or "downward" along the c-axis. This is accounted for by introducing 0.5 occupancies in both possible arrangements. To simplify our discussion, we introduce a notation wherein arrows (↑) and (↓) correspond to the z-coordinate of the hydroxyl group—oxygen being smaller and larger than the z-coordinate of hydrogen, respectively. The pair of hydroxyl groups per primitive cell is denoted by a pair of arrows. In the hexagonal primitive cell, four different orientations, (↑↑), (↑↓), (↓↑), and (↓↓), are possible, with (↑↑) and (↓↓) cells, and (↑↓) and (↓↑) cells being equivalent.

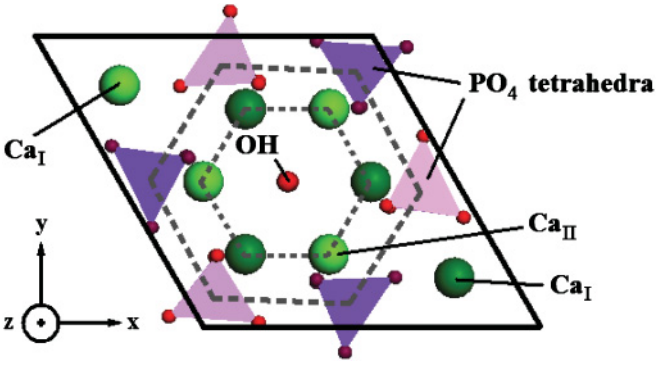

FIG. 3. (Color online) Top view of the hexagonal primitive cell. In the figure, we shifted the original primitive cell in the x and y directions so that the OH column is in the center of the depicted cell. The darker colored Ca_{II} atoms and PO_4 molecules are centered at $z = 0.25c$, and the lighter ones are centered at $z = 0.75c$. The OH column is surrounded by six Ca_{II} atoms and six PO_4 molecules. The Ca_I atoms are now in the corners of the cell. Below both of the two visible Ca_I atoms is a second Ca_I atom at the distance $0.5c$. Here, the lighter Ca_I atom is close to the top face, and the darker Ca_I atom is at $\sim 0.5c$.

To identify the ground state, we calculate the energy of both the (↓↓) and (↓↑) configurations. For later use, we also consider cells in which the hydroxyl molecules are slightly tilted away from the c-axis, keeping the oxygen atoms on the c-axis and OH bond length fixed. These are indicated by (↘↙) if tilted from a (↓↓) configuration and by (↘↖) if tilted from a (↓↑) configuration. Additionally, we consider monoclinic cells created by doubling the hexagonal unit cell in the ***b*** direction. Here, each of the two contributing hexagonal cells is described by one pair of arrows for the OH orientation; for example, (↓↓)(↓↓) or (↓↓)(↑↑) in the simplest cases. The (↓↓)(↓↓) configuration resembles a monoclinic cell, which is reducible to a single hexagonal cell with a (↓↓) configuration. On the other hand, the (↓↓)(↑↑) configuration resembles a monoclinic cell that cannot be reduced further because of the alternating OH orientation in subsequent OH columns.

The binding energies of all models are compared in Fig. 4. The top line in the graph indicates on which reference the unrelaxed cell is based, and arrows indicate the OH configuration before relaxation. The results per hexagonal cell are plotted in ascending energy order. The mixed configuration (↓↓)(↑↑) monoclinic structure suggested by Elliott,[34] yields the lowest energy (structure 1) and is used as the reference energy. The lattice constants are a = 9.53 Å, b = 2a, and c = 6.91 Å. We find the second lowest energy for the hexagonal cell (structure 2) with the lattice constants a = b = 9.53 Å and c = 6.91 Å. The relaxed bond lengths of the hydroxyl and phosphate groups and bonding angles P-O-P of the phosphates in structure 2 are listed in Table I. We find excellent agreement with experimental results.[6,7] During the relaxation of structures

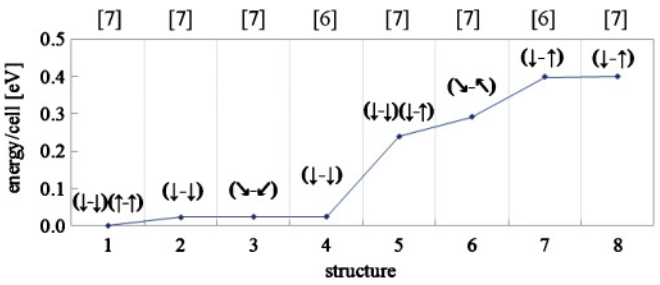

FIG. 4. (Color online) The calculated structures are listed in ascending order according to the binding energy per single cell, and the minimum energy is shifted to zero. We find the lowest binding energy for the monoclinic (↓↓)(↑↑) configuration followed by the hexagonal (↓↓) structure. The energy difference between these two is ~22 meV/cell. The binding energies of structures 2–4 are identical. Structures with flipped OH pairs within the same column generally yield higher binding energy.

TABLE I. Comparison of fully relaxed theoretical bond lengths and bond angles in HA with experimental values.

	Theory	Exp. (Ref. 7)
P-O_I	1.56 Å	1.54 Å
P-O_{II}	1.57 Å	1.55 Å
P-O_{III}	1.55 Å	1.53 Å
O-H	0.977 Å	0.957 Å
O_I-P-O_{II}	111.1°	111.0°
O_I-P-O_{III}	111.6°	111.5°
O_{II}-P-O_{III}	107.5°	107.5°

3 and 4, we find that the OH pairs realign with the c-axis, ending up in structure 2. In structure 6, hydrogen atoms stay at the tilted positions during relaxation, yielding a binding energy that is ∼269 meV/cell higher than the hexagonal ground state structure 2. The (↓↑) type configurations in which OH pairs flip within the same c-column are ∼0.4 eV higher in energy (per hexagonal cell) than the ground state, making them unlikely.

The energy difference between the monoclinic (structure 1) and hexagonal (structure 2) cells is only ∼22 meV per hexagonal cell, suggesting that at room temperature HA can crystallize in a mixed phase with randomly distributed (↓↓) and (↑↑) domains. In the rest of the paper, we will focus on these two structures.

B. Activation energy for the hexagonal to monoclinic transition

The monoclinic phase of HA was first described by Elliott *et al.*,[34] who, following the work by Young,[10] prepared a sample consisting of ∼30% monoclinic HA and 70% hexagonal phases. They concluded that HA grown in a sufficiently clean experimental environment and having few impurities or vacancies can assume monoclinic symmetry under ambient conditions. Later, Hitmi *et al.*[35] found that, while at ambient conditions, both the hexagonal and monoclinic phases can occur. When heated above 470 K, HA always assumes the hexagonal structure, and the transformation is reversible. The overall structural similarity of the monoclinic and hexagonal phases and closeness of the calculated binding energy raise a question of the activation barrier and transition mechanism. To investigate theoretically possible pathways of the transition, we use transition state theory and, more specifically, the nudged elastic band method (NEBM)[36] as implemented in the VASP code.

We start by calculating the energy barrier between two equivalent hexagonal structures, (↓↓) and (↑↑), using hexagonal structure 2 described in section A. We assume that changing the OH configuration from (↓↓) to (↓↑) is unlikely because we have found the latter to be 0.4 eV higher in energy than the former. The transformation involves not only the hydrogen displacement but also that of oxygen (Fig. 5), because the equilibrium positions of oxygen are shifted from the mirror planes at $1/4c$ and $3/4c$, containing Ca triangles. One possible pathway for the transition is to move the hydrogen atoms of the OH molecules along the z-axis. This requires breaking the OH bonds and rebonding hydrogen with the oxygen atom of the adjacent OH molecule

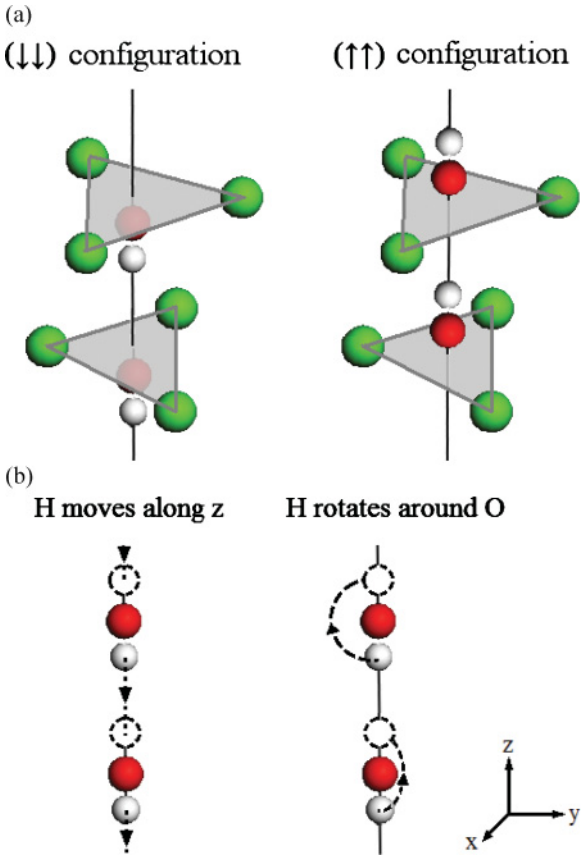

FIG. 5. (Color online) (a) OH positions with respect to the surrounding Ca_{II}-triangles in the (↓↓) and (↑↑) configurations. (b) The figures show two paths of the hydrogen atoms from one equilibrium position to another symmetry-related equilibrium position, thus flipping from (↓↓) to (↑↑).

(Fig. 5). Simultaneously, the oxygen atoms of OH are moved in the opposite direction to their new equilibrium positions. Another possible mechanism is rotating each hydrogen atom around its bonding oxygen while translating the oxygen to its new equilibrium position. The rotation and translation of the hydrogen atom H_i from configuration (↓) to (↑) is described using spherical coordinates as:

$$\vec{r}_{H_i} = \vec{r}_{O(H_i)} + r_{O-H} \begin{pmatrix} \sin(\vartheta)\cos(\varphi_i) \\ \sin(\vartheta)\sin(\varphi_i) \\ \cos(\vartheta) \end{pmatrix} \vartheta = \pi, \ldots, 0. \quad (1)$$

Note that $\vec{r}_{O(H_i)}$ is not constant throughout the transition because the original oxygen atom has to move along the c-axis to its new equilibrium position. The $\vec{r}_{O(H_i)}$ and the angle ϑ are used to create the images for the NEBM to describe the transition pathway. The angle φ_i is given with respect to the $\vec{a}$ lattice vector and is chosen to move the H atoms between two Ca atoms (Fig. 6). This yields two choices:

(i) Rotate hydrogen atom with angles $\varphi_1 = \pi/3$, $\varphi_2 = 4\pi/3$, and move the oxygen atom.

(ii) Rotate hydrogen atom with angles $\varphi_1 = \pi/3$, $\varphi_2 = 2\pi/3$, and move the oxygen atom.

Figure 5 illustrates the linear and rotational transformations, and Fig. 7 shows the calculated energy along these transition

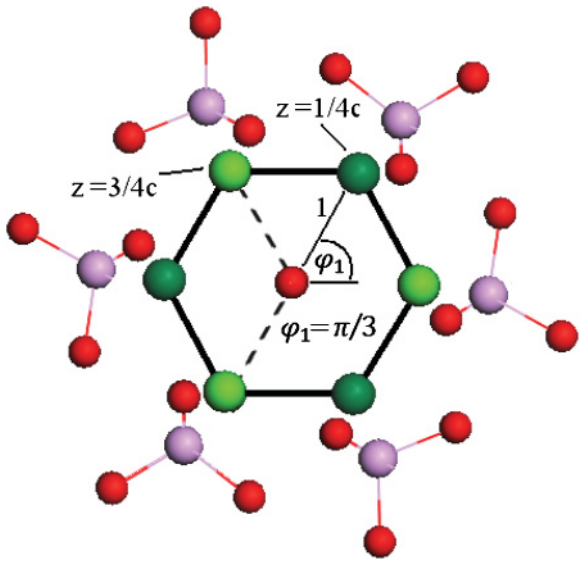

FIG. 6. (Color online) Top view along the OH column surrounded by Ca_{II} and PO_4. The dark Ca atoms are at $z = 1/4c$ and the light ones at $z = 3/4c$. The OH pairs are in the center. There are three equivalent trajectories to flip the top OH pair rotationally. One of them is indicated by projection 1. Once path 1 is selected, there are two inequivalent ways to flip the bottom OH pair, as indicated by the dashed lines.

paths. The energy barriers are 3.5 eV for the linear transition, and 1.3 eV and 1.4 eV in the rotational transitions (i) and (ii), respectively. These result in the activation energy per OH of 1.75 eV, 0.65 eV, and 0.7 eV for the linear and spherical transitions, respectively. The large difference in energy is not surprising because the first mechanism requires breaking the OH bonds. On the other hand, in the rotational flip, no bonds are broken. The barriers for two rotational transitions are very similar and close in energy. In what follows, we only consider the rotational transformation of type (i).

Expanding the potential energy of the rotational transformation to second order around the minimum, we calculate the oscillation frequency of approximately 250 cm^{-1} corresponding to the period of $\tau \approx 134\,fs$. The average time after which a spontaneous flip from $(\downarrow\downarrow)$ to $(\uparrow\uparrow)$ occurs is therefore

$$t_{(\downarrow\downarrow)\rightarrow(\uparrow\uparrow)} = \tau \times N = \tau \times \exp(E_{B,0}/k_BT) \approx 162a \qquad (2)$$

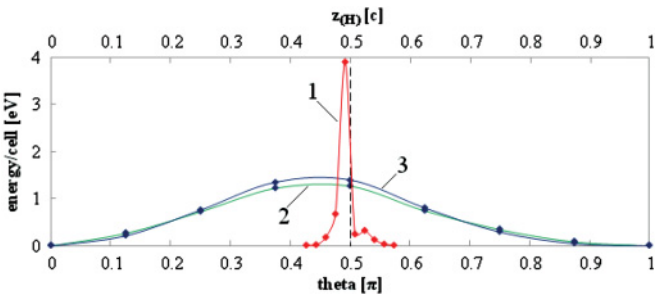

FIG. 7. (Color online) The energy barriers corresponding to the translational (1) and rotational (2 and 3) hydrogen trajectories. The energy barrier for a translational displacement of the hydrogen atoms along the z-axis is approximately three times higher than that of the rotational transition.

at room temperature. In Eq. (2), N is the number of attempts needed to simultaneously flip both OH molecules per unit cell if each attempt has the probability of success of $p = \exp\left(-E_{B,0}/k_BT\right)$. We use $E_{B,0} = 1.3$ eV for the activation energy. The average transition time between the two equivalent hexagonal structures $(\downarrow\downarrow)$ and $(\uparrow\uparrow)$ is 162 years at room temperature.

Now consider the monoclinic cell. Assuming the OH molecules located along the neighboring columns do not interact, the energy barrier for rotational transitions in the monoclinic cell can be written as:

$$\begin{aligned}(\downarrow\downarrow)(\downarrow\downarrow) \rightarrow (\uparrow\uparrow)(\uparrow\uparrow): E_B &= 2E_{B,0}/4 = E_{B,0}/2 = 0.65 \text{ eV} \\ (\downarrow\downarrow)(\downarrow\downarrow) \rightarrow (\downarrow\downarrow)(\uparrow\uparrow): \quad E_B &= E_{B,0}/4 = 0.33 \text{ eV}. \end{aligned} \qquad (3)$$

In Eq. (3), $E_{B,0}$ is the previously calculated energy barrier of 1.3 eV in the hexagonal cell, and E_B is the activation energy per OH pair in the monoclinic cell. Transforming $(\downarrow\downarrow)(\downarrow\downarrow)$ to $(\uparrow\uparrow)(\uparrow\uparrow)$ requires the same energy per OH as flipping $(\downarrow\downarrow)$ to $(\uparrow\uparrow)$. However, the activation energy per OH to transform from $(\downarrow\downarrow)(\downarrow\downarrow)$ to $(\downarrow\downarrow)(\uparrow\uparrow)$ is reduced by a factor of two. The experimentally obtained range for the activation energy to change from hexagonal to monoclinic is 0.016–0.630 eV per OH and 0.84–0.89 eV per OH, reported by Hitmi and Nakamura[35,37] are in qualitative agreement with our results. Hitmi suspected a rotational, whereas Nakamura suspected a linear, transition, explaining why the two ranges are so different. Using classical molecular dynamics, Hochrein *et al.*[38] find 0.52 eV per OH flip in good agreement with our results. Using our calculated activation energy, we write the probability of transformation from $(\downarrow\downarrow)(\downarrow\downarrow)$ to $(\downarrow\downarrow)(\uparrow\uparrow)$ as

$$p = \exp(-E_{B,0}/2k_BT). \qquad (4)$$

Using the same oscillation period as for the hexagonal cell, the average time for the spontaneous hexagonal-monoclinic transition is estimated as

$$t_{(\downarrow\downarrow)(\downarrow\downarrow)\rightarrow(\downarrow\downarrow)(\uparrow\uparrow)} = \tau \times N = \tau \times \exp(E_{B,0}/2k_BT) \approx 26 \text{ ms} \qquad (5)$$

at room temperature. The short transition time suggests that the hexagonal phase would always flip to the monoclinic phase under ambient conditions. Further investigation is needed to explain why the transition from the monoclinic to hexagonal phase occurs at 470 K.

C. Electronic structure

The total electronic density of states (DOS) for both the hexagonal and monoclinic structures is shown in Fig. 8(a). For comparison, we normalize the DOS to the hexagonal cell. The DOS of both structures are very similar, and the following description applies to both phases. Note that we distinguish between the oxygen atoms from the phosphate molecules ($O_{(P)}$) and oxygen atoms from the OH molecules ($O_{(H)}$). The states between −20 eV and −17 eV mainly consist of $O_{(P)}$, $O_{(H)}$, and phosphorous 2s and 3s states, respectively. At −17 eV, the hydrogen 1s states are mixed in. In an ideal PO_4 tetrahedron, the phosphorus sp^3 hybridized orbitals form σ and π bonds with the surrounding oxygen. The σ-type electronic states appear in two peaks within the energy window −8 to −4 eV. In an ideal PO_4 tetrahedron, these σ-states would be closer to each other in energy. However, in the HA crystal,

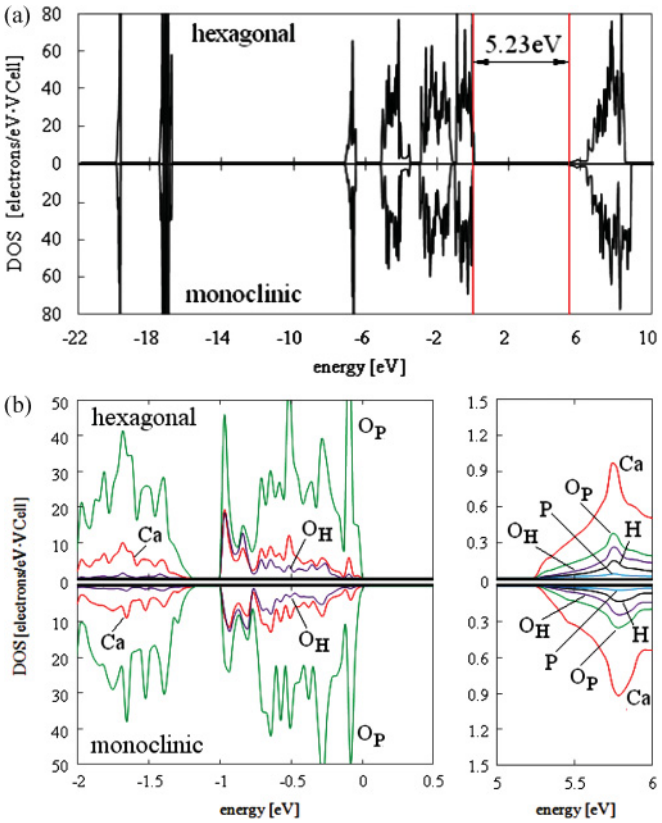

FIG. 8. (Color online) The total DOS (a) and site-projected DOS in the near-gap region (b) of hexagonal and monoclinic HA. The DOS is normalized to a hexagonal cell. The Fermi level is at zero energy. The band gap is 5.23 eV.

the PO_4 tetrahedron is slightly distorted from the ideal 109.5° bonding angle, leading to a split in the energy levels. We find the σ^* electronic states in the conduction band between 6 and 9 eV. The remaining $O_{(P)}$ and $O_{(H)}$ p-states are the main contributors to the DOS between −3 eV and the top of the valence band. Calcium 4s-states contribute mainly between −3 eV and the top of the valence band at zero. In Fig. 8(b), we show the partial DOS projected on the different atomic species in the hexagonal and monoclinic cells in the near gap region. At the bottom of the conduction band, the main contribution is from the s-like states of Ca atoms. The conduction band between 6 and 8 eV is almost entirely made up by unoccupied Ca states, with $l = 2$. In both crystals, the GGA band gap is 5.23 eV, in good agreement with the previously reported LDA band gap of 5.40 eV.[14] The reported experimental values of the band gap range from 3.95 eV[39] to more than 6 eV.[40] Our calculations suggest a large band gap, considering that GGA underestimates the gap. Because the DOS of the hexagonal and monoclinic phase appear very similar, we only calculate the band structure for the smaller hexagonal cell. In Fig. 9, we show the calculated band structure along the high-symmetry directions in the Brillouin zone in the near-gap region. First, we notice that HA is an indirect gap material. The valence band top shows little dispersion, indicating heavy localized holes. We find two energy maxima in the valence band separated by only 8 meV. The top of the valence band (shifted to 0 eV) occurs along the Γ to K line. The bottom of the conduction

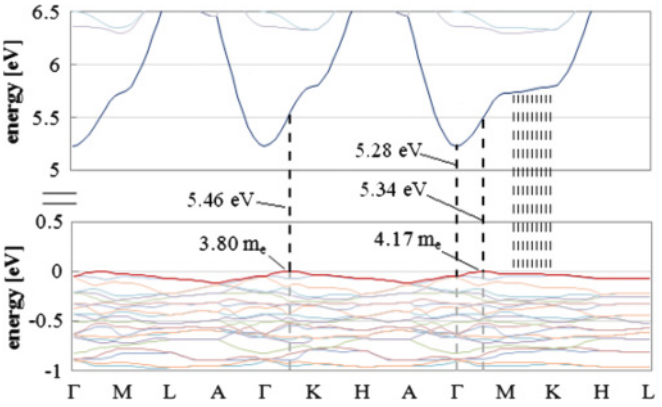

FIG. 9. (Color online) The electronic band structure of hexagonal HA in the near-gap region. The energy range in the gap region is not shown for clarity. The band structure suggests that HA is an indirect band material. The lowest energy optical excitations are indicated. The dashed lines between M and K indicate nearly constant energy optical excitations.

band is at the Γ-point, and shows a free electron character with the anisotropic effective mass. Fitting the bottom of the conduction band at Γ to a second-order polynomial, we calculate the effective electron mass tensor:

$$(m^*_{\alpha\beta}) = \hbar^2 \left[\frac{d^2E}{dk_\alpha dk_\beta}\right]^{-1} = \begin{pmatrix} 0.61 & -0.01 & -0.01 \\ -0.01 & 0.61 & -0.01 \\ -0.01 & -0.01 & 0.48 \end{pmatrix} \times m_e. \tag{6}$$

The principal values are 0.48, 0.60, and 0.62 in units of the electron mass. The indirect band gap is 5.23 eV. The direct transitions at the top of the valence band and at the Γ-point are at 5.46 and 5.28 eV, respectively. Another interesting feature is the flat region in both the valence and conduction bands along the M to K line. With the excitation energy of 5.75 eV, this feature should be noticeable in optical adsorption. Unfortunately, no experimental data are available. When comparing our results with the band structure calculated by Rulis *et al.*[15] in Fig. 10, we notice slight differences. The most notable one is the energy gap. Rulis calculates 4.5 eV versus our 5.3 eV. We attribute the discrepancy to a different basis (Rulis uses the linear combination of atomic orbitals). The overall band structure and near-parabolic dispersion at the bottom of the conduction band agree well with their results.

D. Phonon eigenmodes at the Γ-point

Experimental studies of hydroxyapatite vibrational properties remain scarce. The most recent papers are those of Fowler *et al.*[41] and Markovic *et al.*[42] reporting the infrared (IR) and Raman active vibrational modes, respectively. Theoretical studies of the HA vibrational spectra are quite difficult due to the crystal's complexity, and are typically limited to classical shell models.[43] However, the results strongly depend on the model potentials that have to be fitted to match the experimental data (a comparison of different sets of parameters is given by Calderin[43]). Therefore, a more general and transferrable approach of calculating the phonon spectrum is desirable. We use DFT to calculate the vibrational

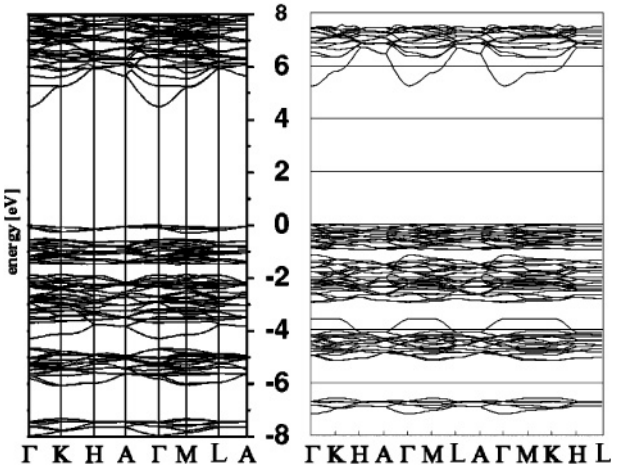

FIG. 10. The band structure of hexagonal HA from Ref. 15 (left) compared with our band structure (right).

eigenmodes of hexagonal HA at the Γ-point. We analyze the influence of the ionic nature (long range Coulomb interactions) of the crystal on the eigenmodes and identify the vibrational modes mostly affected by the long range effects.

To calculate the short-range force constant matrix we take the numerical derivative of the Hellmann-Feynman forces with respect to small ionic displacements (e.g., Ref. 44). The lattice Fourier transform of the force constant matrix yields the dynamical matrix:[44,45]

$$\vec{D}(\vec{k};\mu,\nu) = \frac{1}{\sqrt{M_\mu M_\nu}} \sum_m \vec{B}\,(0,\mu;m,\nu) \times \exp\{2\pi i \vec{k} \times [\vec{R}\,(0,\mu) - \vec{R}\,(m,\nu)]\}. \quad (7)$$

$\vec{R}(0,\mu)$ is the position of atom μ in the 0th primitive cell within the supercell. $\vec{R}(m,\nu)$ is the position of atom ν in the mth unit cell. $\vec{B}(0,\mu;m,\nu)$ are the force constants relating atoms $(0,\mu)$ and (m,ν). M_μ and M_ν are the masses of atoms ν and μ. In three-dimensional space, the dimension of the dynamical matrix is $3N \times 3N$, where N is the number of atoms in the primitive cell. Since we are interested in phonons at the Γ-point we only calculate the forces in a single hexagonal primitive cell. In covalent systems, the range of interaction is assumed to be finite, and the dynamical matrix can be directly calculated using the Hellmann–Feynman forces acting on the ions in the supercell when displacing one atom from its equilibrium position. In the ionic system, one has to worry about long-range dipole-dipole interactions. This is accomplished by adding a long-range correction to the dynamical matrix given by:[44]

$$\vec{D}^{\,\text{long}}_{\alpha\beta}(\vec{k};\mu,\nu) = \frac{e^2}{V\varepsilon_0\varepsilon_\infty} \frac{[\vec{k}\,\vec{\vec{Z}}^*(\mu)]_\alpha [\vec{k}\,\vec{\vec{Z}}^*(\nu)]_\beta}{|\vec{k}|^2} \times \exp\left(-\frac{|\vec{k}|^2}{\rho^2}\right). \quad (8)$$

Here, we use SI units. $\vec{\vec{Z}}$ is the Born effective charge tensor of atom μ, and V is the volume of the primitive cell. The long-range contribution only affects the phonon modes close to the Γ-point. The Born effective charge tensors introduce a directional dependence in Eq. (8). The total dynamical matrix is given by a sum of Eqs. (7) and (8).

First, we calculate the phonon eigenmodes in HA at the Γ-point without the long-range correction. We use a single primitive hexagonal cell. There are 132 eigenmodes, including Raman and IR active vibrations. We use our calculated eigenmodes to approximate the phonon density of states (PDOS) at the Γ-point given by:

$$\frac{\#\ \text{of Eigenmodes}}{\Delta f} = \sum_i \delta(f - f_i) \equiv N(f), \quad (9)$$

The DOS is a sum of delta-functions positioned at the calculated eigenmodes at each k-point. We represent these peaks by a Gaussian, and apply a Gauss broadening of $\sigma = 15\ \text{cm}^{-1}$. In Fig. 11, we compare our results with the DOS constructed using experimental IR and Raman active modes as reported by Fowler[41] and Markovic.[42] The calcium ions contribute predominantly to the low frequency modes. In the ranges from 350 to 650 cm^{-1} and from 850 to 1100 cm^{-1}, mainly the PO_4 molecules contribute to the spectrum. The OH modes are at 693 and 3660 cm^{-1}, corresponding to the OH's libration and stretching modes, respectively. Compared with the experimental work, we find good qualitative agreement. The frequencies corresponding to the phosphate eigenmodes are underestimated by ∼5%–10%. This is consistent with the observation that the theoretical PO bond length is 0.02–0.03 Å longer than the experimental value. On the other hand, theoretical eigenmodes of the OH groups at 693 cm^{-1} (libration mode in x and y directions) and 3660 cm^{-1} (OH stretching mode) are overestimated by ∼5%–10% compared with experimental results.

Having found reasonable agreement with experimental results without considering the long-range interactions, we now include the long-range correction (Eq. (8)). We approach the Γ-point along the M to Γ, K to Γ, and A to Γ directions. These directions correspond to approaching Γ from the face center, corner, and top of the hexagonal Brillouin zone. Experimentally, the high-frequency dielectric constant is sensitive to the Ca/P ratio of the crystal (e.g., Ref. 46). The values for ε_∞ in the literature for stoichiometric HA with the Ca/P ratio 1.67 vary be-

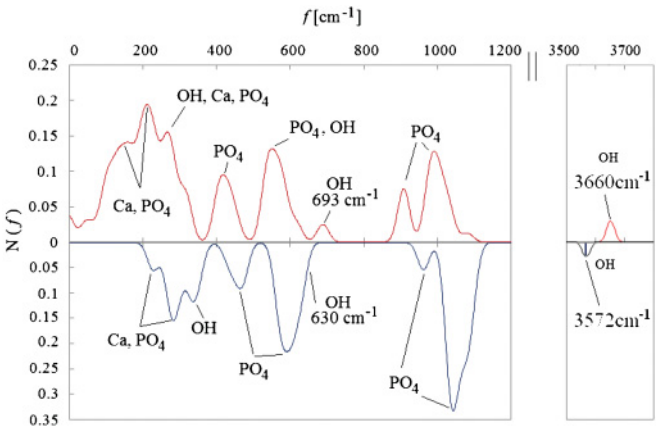

FIG. 11. (Color online) The theoretical phonon density of states at the Γ-point compared with the experimental IR and Raman active modes. Our Ca and PO_4 peaks are underestimated by ∼10%, whereas the OH modes are overestimated by ∼10%.

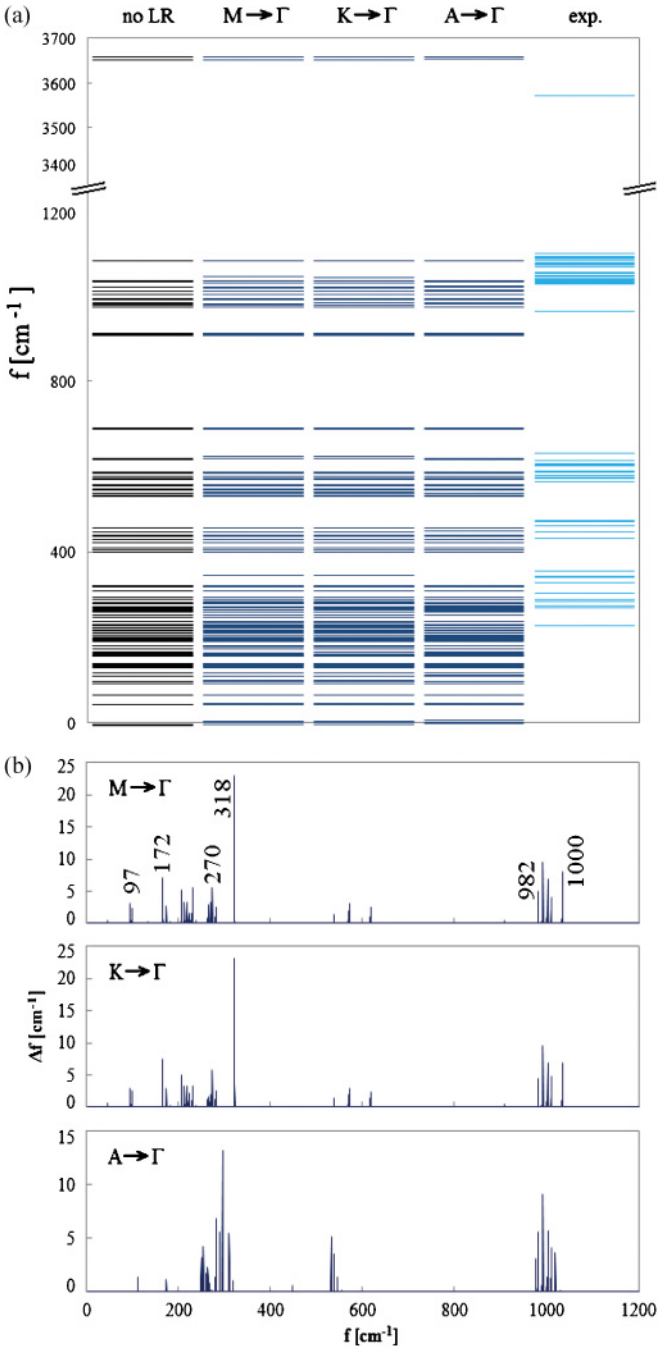

FIG. 12. (Color online) (a) The phonon frequencies at the Γ-point with and without the long-range correction. When applying the long-range correction, we consider approaching the Γ-point from the M-point, the K-point, and the A-point, corresponding to the directions (100), (110), and (001). We use the experimental values from Fowler and Markovic (Refs. 41 and 42). The direction of approach has little influence on the eigenmodes. The deviation from the experimental values is about 10%. (b) The change in the phonon frequency when applying the long-range correction. We find almost identical changes when approaching along the (100) and the (110) direction (M to Γ and K to Γ, respectively). The largest change occurs for the mode at 318 cm^{-1}, which corresponds to a pure OH libration mode. In the (001) direction (A→Γ), this mode is nearly unaffected by the long-range correction.

tween $\varepsilon_\infty = 5$ and $\varepsilon_\infty = 20$,[46–50] in part because of the variation in porosity and the water content of the samples, and in part to too low a frequency of measurement. In this work, we use $\varepsilon_\infty = 5$ and cross-check with $\varepsilon_\infty = 7$ to see the qualitative dependency of the eigenmodes on ε_∞. The calculated Born effective charge tensors are summarized in Table II. For the Gaussian smearing in (Eq. (8)), we use $\rho = 0.02$ Å^{-2}. We plot our results in Fig. 12(a), along with the experimentally measured modes. We find that including the long-range correction has little effect on most of the vibration modes in good agreement with Calderin's work,[43] where a shell model was used to calculate the phonons when approaching the Γ-point from the (100) and the (001) direction. In Fig. 12(b), we show the difference between the long-range corrected spectrum and uncorrected spectrum below 1200 cm^{-1} at the Γ-point. Positive Δf means the long-range corrected modes are higher in frequency. The frequency shifts are very similar when approaching along the (100) direction and the (110) direction (M to Γ and K to Γ), ranging from 1 to 25 cm^{-1}. When approaching along the (001) direction (A to Γ), somewhat different eigenmodes shift compared with approaching along (100) and (110), and the peak at 318 cm^{-1} virtually disappears. While in the modes between 97 and 318 cm^{-1}, all atoms in the cell are vibrating; the 318 cm^{-1} mode is a pure OH libration mode in the x-y plane. The remaining shifted modes close to 600 cm^{-1} and around 1000 cm^{-1} are pure PO_4 vibration modes. The change in frequency due to the long-range correction is most notable for the OH mode at 318 cm^{-1}, which moves up to 343 cm^{-1}

TABLE II. Born effective charge tensors for the different atomic sites.

	Born effective charge
H	$\begin{pmatrix} 0.37 & -0.01 & 0 \\ 0.01 & 0.37 & 0 \\ 0 & 0 & 0.28 \end{pmatrix}$
P	$\begin{pmatrix} 3.17 & 0.04 & 0 \\ -0.01 & 3.17 & 0 \\ 0 & 0 & 3.08 \end{pmatrix}$
Ca_I	$\begin{pmatrix} 2.41 & -0.08 & 0 \\ 0.08 & 2.41 & 0 \\ 0 & 0 & 2.51 \end{pmatrix}$
Ca_{II}	$\begin{pmatrix} 2.45 & 0.02 & 0 \\ -0.01 & 2.45 & 0 \\ 0 & 0 & 2.46 \end{pmatrix}$
O_I	$\begin{pmatrix} -1.93 & 0.03 & 0 \\ -0.02 & -1.93 & 0 \\ 0 & 0 & -1.41 \end{pmatrix}$
O_{II}	$\begin{pmatrix} -1.92 & 0 & 0 \\ 0 & -1.91 & 0 \\ 0 & 0 & -1.30 \end{pmatrix}$
O_{III}	$\begin{pmatrix} -1.47 & -0.02 & 0 \\ 0.02 & -1.47 & 0 \\ 0 & 0 & -2.13 \end{pmatrix}$
O_H	$\begin{pmatrix} -1.71 & 0.04 & 0 \\ -0.04 & -1.71 & 0 \\ 0 & 0 & -0.94 \end{pmatrix}$

TABLE III. Calculated elastic constants and bulk modulus compared with other theoretical calculations and corresponding experimental values. The bulk modulus is related to the elastic constants by the formula $B = \frac{2}{9}\left(C_{11} + C_{12} + 2C_{13} + C_{33}/2\right)$.

Constant (10^{11} dyn/cm^2)	This work	Ref. 53	Pseudo-exp. (Ref. 52)
C_{11}	12.90	15.75	13.70
C_{12}	3.70	5.74	4.25
C_{13}	6.70	5.97	5.49
C_{33}	17.30	14.73	17.20
C_{44}	4.40	4.39	3.96
B	8.60	9.07	8.90

when approaching Γ from the M-point. Using $\varepsilon_\infty = 7$ in the long-range correction, this OH mode moves up to 335 cm^{-1}, being the only mode substantially affected by using $\varepsilon_\infty = 5$. Overall, we find good agreement between our phonon spectra and experimental results.

E. Elastic constants of HA

The anisotropy of the elastic properties of bones is governed by their main constituents, HA, the collagen chains, and water. The theoretical determination of the elastic properties of composite materials is often done by averaging the elastic properties of the separate materials. Although the quality of the results fluctuates depending on the material in question, upper and lower bounds of the effective moduli of composites can be found rigorously.[51] Previously, Katz and Ukraincik[52] calculated a set of pseudo-single crystal elastic constants extracted from the measured elastic constants of fluorapatite. The validity of such a calculation is somewhat justified by a strong similarity of the crystal structures of these two materials. Mustafa *et al.*[53] use a force field approach to obtain the elastic constants of HA. Here, we calculate the elastic constants of hexagonal HA from first-principles.

Generally, the energy of a strained system can be written as a second-order Taylor expansion in the distortion parameters $\alpha_{i,j}$:

$$E(V,\alpha) = E(V_0,0) + \frac{V_0}{2}\sum_{a,b,c,d} C_{abcd}\alpha_{ab}\alpha_{cd}. \qquad (10)$$

The first-order term drops out as the expansion is at about the ground state. The second-order term is described by the adiabatic elastic constants C_{abcd}. However, the C_{abcd} and α_{ab} are not all independent, and using Voigt notation, Eq. (10) can be written as

$$E(V,\alpha) = E(V_0,0) + \frac{V_0}{2}\sum_{i,j} C_{ij}\alpha_i\xi_i\alpha_j\xi_j. \qquad (11)$$

The introduced factors ξ_i account for the symmetry of the α's, $\alpha_{ab} = \alpha_{ba}$ (i.e., for $b \neq a$, both α_{ab} and α_{ba} are labeled with the same Voigt index). Therefore, we get $\xi_i = 1$ if the Voigt index is 1, 2, or 3 and $\xi_i = 2$ if the Voigt index is 4, 5, or 6.[54]

There are five independent elastic constants in a hexagonal crystal: C_{11}, C_{12}, C_{13}, C_{33}, $C_{44} = C_{55}$. To determine these constants, five independent stresses must be applied to the system (see the Appendix). Distortions (I), (III), and (V) keep hexagonal symmetry in the strained cell. Distortion (II) creates a monoclinic cell, and distortion (IV) creates a cell with triclinic symmetry. Equation (11) is valid for small distortions. To have a measure of "small," we compare the volume changes after applying a specific distortion. Distortions (I) and (V) yield the largest change in volume. Thus, for (I), we use the parameters $\alpha = -0.01, -0.005, 0.00, 0.005$, and 0.01, and for (V) we apply $\alpha = -0.005, -0.0025, 0.00, 0.0025$, and 0.005. For distortions (II)–(IV), we use $\alpha = -0.02, -0.01, 0.00, 0.01$, and 0.02. These choices of α ensure that the change in volume relative to the equilibrium volume V_0 is smaller than 15 Å^3 or ∼2.8% of V_0. For all distortions, we use a quadratic fit to extract the elastic constants C_{ij}. Our results are summarized in Table III. For C_{11}, C_{33}, and the bulk modulus B, we find agreement within ∼6% of the values previously reported by Katz and Mostafa.[52,53] Our C_{12}, C_{13}, and C_{44} are within ∼21% of Katz's and Mostafa's results, indicating overall good qualitative agreement.

IV. CONCLUSIONS

Using density functional theory, we find that the ground state of hydroxyapatite is monoclinic, in agreement with previous calculations[13] and recent experiments.[35,37] The hexagonal phase is only 22 meV higher in energy than the monoclinic ground state. The structural transition path from the monoclinic to the hexagonal crystal phase and vice versa most likely involves the rotation of hydroxyl groups, as suggested by Hitmi.[35] The activation energy for such a transition is 0.33 eV per OH molecule, and the transition time at room temperature is ∼26 ms. We find close similarity in the electronic structure of both phases, suggesting similar chemical properties. For the hexagonal phase, in agreement with previous theoretical results, we find the indirect band gap 5.23 eV. The bottom of the conduction band mainly consists of Ca s-states and shows free-electron-like behavior with the anisotropic mass at the Γ-point. Our results for the vibrational eigenmodes at the Γ-point are within ±10% of available experimental results,[41,42] and calculated elastic constants agree well with the experimental results reported by Katz[52] and Mostafa.[53]

ACKNOWLEDGMENTS

This work was supported by the National Science Foundation under Grant DMR1006725 and by the Texas Advanced Computing Center.

APPENDIX

Following the approach described by Fast *et al.*,[55] we use five independent distortions to obtain the elastic constants of the hexagonal cell. Their action on the crystal structure and symmetry are explained in the section E. The small parameter α describes the deviation of the distorted crystal from the

original one.

$$e_{\mathrm{I}} = \begin{pmatrix} 1+\alpha & 0 & 0 \\ 0 & 1+\alpha & 0 \\ 0 & 0 & 1 \end{pmatrix}$$

$$e_{\mathrm{II}} = \begin{pmatrix} 1+\alpha & 0 & 0 \\ 0 & 1-\alpha & 0 \\ 0 & 0 & 1 \end{pmatrix}$$

$$e_{\mathrm{III}} = \begin{pmatrix} 1 & 0 & 0 \\ 0 & 1 & 0 \\ 0 & 0 & 1+\alpha \end{pmatrix}$$

$$e_{\mathrm{IV}} = \begin{pmatrix} 1 & 0 & \alpha \\ 0 & 1 & 0 \\ \alpha & 0 & 1 \end{pmatrix}$$

$$e_{\mathrm{V}} = \begin{pmatrix} 1+\alpha & 0 & 0 \\ 0 & 1+\alpha & 0 \\ 0 & 0 & 1+\alpha \end{pmatrix} \tag{A1}$$

*demkov@physics.utexas.edu

[1] C. A. Van Blitterswijk, J. J. Grote, W. Kuijpers, W. T. Daems, and K. A. de Groot, Biomaterials **7**, 553 (1986).
[2] A. L. Boskey, *The Organic and Inorganic Matrices* (CRC Press, Washington, 2004), pp. 91–123.
[3] A. Kruse, R. E. Jung, F. Nicholls, R. A. Zwahlen, C. H. F. Hämmerle, and F. E. Weber, Clin. Oral Impl. Res. **22**, 506 (2011).
[4] B. Leon and J. A. Janson, *Thin Calcium Phosphate Coatings for Medical Implants* (Springer, New York, 2009).
[5] W. J. Schmidt, Naturwissenschaften **24**, 361 (1936).
[6] A. S. Posner, A. Perloff, and A. F. Diorio, Acta Cryst. **11**, 308 (1958).
[7] M. I. Kay and R. A. Young, Nature **204**, 1050 (1964).
[8] S. Weiner and P. A. Price, Calcif. Tissue Int. **39**, 365 (1986).
[9] E. M. Carlisle, Science **167**, 179 (1970).
[10] R. A. Young, Trans. N. Y. Acad. Sci. **29**, 949 (1967).
[11] H. Morgan, R. M. Wilson, J. C. Elliott, S. E. P. Dowker, and P. Anderson, Biomaterials **21**, 617 (2000).
[12] G. Ma and X. Y. Liu, Cryst. Growth Des. **9**, 2991 (2009).
[13] N. H. de Leeuw, Chem. Commun. 1646 (2001).
[14] L. Calderin, M. J. Stott, and A. Rubio, Phys. Rev. B **67**, 134106 (2003).
[15] P. Rulis, L. Ouyang, and W. Y. Ching, Phys. Rev. B **70**, 155104 (2004).
[16] H. F. Chappell and P. D. Bristowe, J. Mater. Sci. **18**, 829 (2007).
[17] N. H. de Leeuw, Royal Society of Chemistry **20**, 5376 (2010).
[18] S. Yin and D. E. Ellis, Phys. Chem. Chem. Phys. **12**, 156 (2010).
[19] J. Terra, E. Rodrigues Dourado, J.-G. Eon, D. E. Ellis, G. Gonzalez, and A. M. Rossi, Phys. Chem. Chem. Phys. **11**, 568 (2009).
[20] L. Calderin, D. Dunfield, and M. J. Stott, Phys. Rev. B **72**, 224304 (2005).
[21] M. Corno, A. Rimola, V. Bolis, and P. Ugliengo, Phys. Chem. Chem. Phys. **12**, 6309 (2010).
[22] H. F. Chappell, M. Duer, N. Groom, C. Pickard, and P. D. Bristowe, Phys. Chem. Chem. Phys. **10**, 600 (2008).
[23] N. Almora-Barrios, K. F. Austen, and N. H. de Leeuw, Langmuir **25**, 5018 (2009).
[24] D. K. Dubey and V. Tomar, Acta Biomaterialia **5**, 2704 (2009).
[25] R. Astala and M. J. Stott, Phys. Rev. B **78**, 075427 (2008).
[26] G. Kresse and J. Hafner, Phys. Rev. B **47**, 558 (1993).
[27] G. Kresse and J. Furthmüller, Comput. Mat. Sci. **6**, 15 (1996).
[28] G. Kresse and J. Furthmüller, Phys. Rev. B **54**, 11169 (1996).
[29] G. Kresse and J. Hafner, J. Phys: Condens. Matt. **6**, 8245 (1994).
[30] G. Kresse and D. Joubert, Phys. Rev. B **59**, 1758 (1999).
[31] J. P. Perdew, J. A. Chevary, S. H. Vosko, K. A. Jackson, M. R. Pederson, D. J. Singh, and C. Fiolhais, Phys. Rev. B **46**, 6671 (1992).
[32] P. E. Blöchl, Phys. Rev. B **50**, 17953 (1994).
[33] H. J. Monkhorst and J. D. Pack, Phys. Rev. B **13**, 5188 (1976).
[34] J. C. Elliott, P. E. Mackie, and R. A. Young, Science **180**, 1055 (1973).
[35] N. Hitmi, C. LaCabanne, and R. A. Young, J. Phys. Chem. Solids **47**, 533 (1986).
[36] H. Jonsson, G. Mills, and K. W. Jacobsen, in *Classical and quantum dynamics in condensed phase simulations*, edited by B. J. Berne, G. Ciccotti, and D. F. Coker (World Scientific, Singapore, 1998), p. 385.
[37] S. Nakamura, H. Takeda, and K. Yamashita, J. Appl. Phys. **89**, 5386 (2001).
[38] O. Hochrein, R. Kniep, and D. Zahn, Chem. Mater. **17**, 1978 (2005).
[39] G. Rosenman, D. Aronov, L. Oster, J. Haddad, G. Mezinskis, I. Pavlovska, M. Chaikina, and A. Karlov, J. Lumin. **122–123**, 936 (2007).
[40] M. Tsukada, M. Wakamura, N. Yoshida, and T. Watanabe, J. Mol. Cat. A **338**, 18 (2011).
[41] B. O. Fowler, Inorg. Chem. **13**, 194 (1973).
[42] M. Markovic, B. O. Fowler, and M. S. Tung, J. Res. Natl. Inst. Stand. Technol. **109**, 553 (2004).
[43] L. Calderin, D. Dunfield, and M. J. Stott, Phys. Rev. B **72**, 224304 (2005).
[44] S. Baroni, S. Gironcoli, A. Dal Corso, and P. Giannozzi, Rev. Mod. Phys. **73**, 515 (2001).
[45] M. Born and K. Huang, *Dynamical theory of crystal lattices* (Oxford University Press, Oxford, 1962).
[46] M. Quilitz, K. Steingroever, and M. Veith, J. Mater. Sci.: Mater. Med. **21**, 399 (2010).
[47] C. C. Silva, H. H. B. Rocha, F. N. A. Freire, M. R. P. Santos, K. D. A. Saboia, J. C. Goes, and A. S. B. Sombra, Mat. Chem. Phys. **92**, 260 (2005).
[48] T. P. Hoepfner and E. D. Case, J. Biomed. Mater. Res. **60**, 643 (2002).
[49] T. Ikoma and A. Yamazaki, J. Mater. Sci. Lett. **18**, 1225 (1999).

[50]J. P. Gittings, C. R. Bowen, A. C. E. Dent, I. G. Turner, F. R. Baxter, and J. B. Chaudhuri, Acta Biomaterialia **5**, 743 (2009).
[51]G. W. Milton, Phys. Rev. Lett. **46**, 542 (1981).
[52]J. L. Katz and K. Ukraincik, J. Biomechanics **4**, 221 (1971).
[53]N. Y. Mostafa and P. W. Brown, J. Phys. Chem. Solids **68**, 431 (2007).
[54]D. C. Wallace, Solid State Phys. **25**, 302 (1970).
[55]L. Fast, J. M. Wills, B. Johansson, and O. Eriksson, Phys. Rev. B **51**, 17431 (1995).